2014

FROM CARDIAC OPTICAL IMAGING DATA TO BODY SURFACE ECG: A THREE DIMENSIONAL VENTRICLE MODEL

Yihua Zhao
University of Kentucky, zhyh8341@gmail.com

STUDENT AGREEMENT:

I represent that my thesis or dissertation and abstract are my original work. Proper attribution has been given to all outside sources. I understand that I am solely responsible for obtaining any needed copyright permissions. I have obtained and attached hereto needed written permission statement(s) from the owner(s) of each third-party copyrighted matter to be included in my work, allowing electronic distribution (if such use is not permitted by the fair use doctrine).

I hereby grant to The University of Kentucky and its agents the irrevocable, non-exclusive, and royalty-free license to archive and make accessible my work in whole or in part in all forms of media, now or hereafter known. I agree that the document mentioned above may be made available immediately for worldwide access unless a preapproved embargo applies. I retain all other ownership rights to the copyright of my work. I also retain the right to use in future works (such as articles or books) all or part of my work. I understand that I am free to register the copyright to my work.

REVIEW, APPROVAL AND ACCEPTANCE

The document mentioned above has been reviewed and accepted by the student's advisor, on behalf of the advisory committee, and by the Director of Graduate Studies (DGS), on behalf of the program; we verify that this is the final, approved version of the student's dissertation including all changes required by the advisory committee. The undersigned agree to abide by the statements above.

Yihua Zhao, Student

Dr. Abhijit Patwardhan, Major Professor

Dr. Abhijit Patwardhan, Director of Graduate Studies

FROM CARDIAC OPTICAL IMAGING DATA TO BODY SURFACE ECG: A THREE DIMENSIONAL VENTRICLE MODEL

THESIS

A thesis submitted in partial fulfillment of the requirements
for the degree of Master of Science in Biomedical Engineering
in the College of Engineering at the University of Kentucky

By

Yihua Zhao

Lexington, Kentucky

Director: Dr. Abhijit Patwardhan

Lexington, Kentucky

2014

ABSTRACT OF THESIS

FROM CARDIAC OPTICAL IMAGING DATA TO BODY SURFACE ECG:

A THREE DIMENSIONAL VENTRICLE MODEL

Understanding the mechanisms behind unexplained abnormal heart rhythms is important for diagnosis and prevention of arrhythmias. Many studies have investigated the mechanisms at organ, tissue, cellular and molecular levels. There is considerable information available from tissue level experiments that investigate local action potential properties and from optical imaging to observe activity propagation properties at an organ level. By combining those electrophysiological properties together, in the present study we developed a simulation model that can help in estimation of the resulting body surface potentials from a specific electrical activity pattern within the myocardium. Some of the potential uses of our model include: 1) providing visualization of an entire electrophysiological event, i.e. surface potentials and associated source which would be optical imaging data, 2) estimation of QT intervals resulting from local action potential property changes, 3) aiding in improving defibrillation therapy by determining optimal timing and location of shocks.

KEYWORDS: electrophysiology, ventricle model, arrhythmia, 12-lead ECG, optical data

Yihua Zhao

July 2014

FROM CARDIAC OPTICAL IMAGING DATA TO BODY SURFACE ECG:

A THREE DIMENSION VENTRICLE MODEL

By

Yihua Zhao

Dr. Abhijit Patwardhan
Director of Thesis

Dr. Abhijit Patwardhan
Director of Graduate Studies

August 31st, 2014

ACKNOWLEDGEMENTS

My deepest gratitude goes first and foremost to Dr. Abhijit Patwardhan, my advisor, for his constant encouragement guidance, patience, and friendship during my graduate studies at University of Kentucky. He encourages me to not only grow as an engineer, but also as an instructor and independent thinker. He also gives me the opportunity to take an internship in my last semester. I do not think that many graduate students are given the opportunity to develop their own individuality with such independent. I clearly remembered that one of my colleagues walked by my seat and said “I never see a teacher making comments on student’s draft so carefully”. Without his guidance and persistent help, I could not make such progress in past three years. Without his nurturing and assistance, I could not have made the program done so smoothly.

I also would like to thank the members on my committee, Dr. Sunderam and Dr. Shin, for their instruction and valuable discussion during my program.

Finally, I give my sincere thanks to my parents and other family members. Though thousands miles away from the U.S., they have constantly supported, encouraged and believed in me during my study oversea.

CONTENTS

LIST OF FIGURES

CHAPTER ONE: INTRODUCTION

One of the most serious health problems affecting large groups of people in developed and developing world is related to the malfunction of the heart, which has been a major cause of morbidity and mortality. Among the various consequences of heart malfunction, some types of ventricular arrhythmia are dangerous and may occur in people without any warning. Some arrhythmias do not cause symptoms. The former types of arrhythmias usually are associated with harmful events, like a higher risk of blood clotting or insufficient blood transportation, and can even lead to sudden cardiac death [1]. According to a report from American Heart Association, in the western world alone atrial fibrillation and flutter account for approximately 25% of strokes while ventricular tachycardia and fibrillation account for the majority of sudden deaths experienced in this population [2].

In the clinic, arrhythmia is usually first detected by these simple but nonspecific means, like auscultation of the heartbeat with a stethoscope, or feeling for peripheral pulses. This preliminary detection can give the doctor a general indication of the heart rate and whether the cardiac rhythm is regular or irregular. Electrocardiogram (ECG) is the simplest specific diagnostic test for assessment of arrhythmia. A trained clinician can read a sequence of heart beats and interpret it with the patient's symptoms. Since arrhythmias may not always be associated with symptoms and may not exist for a long period of time, not all arrhythmias or potential of arrhythmias can be detected by ECG testing, thus clinicians are not able to accurately interpret the results or predict the risk of arrhythmia. In recent years, various non invasive imaging techniques have been developed to assist the diagnosis, such as magnetic resonance imaging (MRI) and cardiac ultrasound. For instance, Sharma (2013) concluded that cardiac MRI could help identify the possible cause of sudden cardiac arrest in more than 50% of resuscitated patients, and Parga (2014) reported that MRI is a promising technique to visualize the coronary artery tree and to diagnose congenital coronary artery fistula [3,4]. By combining imaging techniques with traditional ECG measurements, the principal functional and morphological features of heart can be assessed better, but the difficulties in predicting and preventing

arrhythmias still exist [5-8].

As the detection equipment becomes more complex and analysis tools become more sophisticated, doctors and researchers do have clearer understanding of structure and function of the heart. What many researches are curious about for long time is the mechanism of arrhythmias. There are a number of factors that may make a person prone to arrhythmias. For instance, a group of abnormally depolarizing cells or islands of electrically inert tissue can cause arrhythmias. It remains unclear as to why abnormal firing cells at a specific location at one specific instant trigger abnormal heart rhythm, but not others. Thus, it is not clear what types of abnormal heart rhythm finally lead to arrhythmias. However, understanding the mechanisms behind those unexplained abnormal heart rhythms is important for diagnosis and prevention of arrhythmias.

Since arrhythmia is an organ level phenomenon, many studies explore the phenomenon at lower levels to determine mechanisms at organ, tissue, cellular and molecular levels. Invasive experimental study is a very useful method of evaluating the electrical properties of cardiac cells and tissues, while ECG measurements reflect the integrated electrical activity of the entire heart. A bridge linking the research results of invasive experiments, such as action potential analysis at the level of single cells with body surface ECG measurements will provide a more comprehensive knowledge of the relationship between characteristics of the action potentials and the surface ECG. Dr. Rudy's group, in Case Western Reserve University, and Dr. Oosterom's group, in Radboud University Medical Center, have reported some very elegant studies in this field [9-11].

In previous studies conducted in our group, we have recorded large number of action potential samples from cardiac cells of pigs, dogs, mice and human, and have collected considerable amount of optical mapping data from pig heart [12,13]. In a previous study, we also recorded pseudo-ECG of isolated hearts simultaneously with optical data. In the present study, our objective was to combine these electrophysiological signals and develop a simulation model that enables estimation of the resulting body surface potential maps from a specific electrical activity pattern within the myocardium. In addition, we tried to improve the user interface so that the model can present a vivid demonstration of

electrical activity in almost real time.

In this study, the original geometry is based on MRI data and geometry files downloaded from the ECGSIM website [14]. We modified the polygon mesh for the geometry to make it smoother. Optical mapping data was acquired in our previous heart perfusion experiments and action potential samples were collected in previous pig heart tissue experiments. The 3D display of the developed model relies on OpenGL with Qt GUI application [15].

CHAPTER TWO: BACKGROUND

2.1 Cardiac Cycle

An individual complete heartbeat is also called a cardiac cycle. As described in Levy & Koeppen's textbook (2010) [1617], the cardiac cycle usually includes two stages: systole and diastole. By convention, a cardiac cycle begins at the end diastole when the pressure in left ventricle increases without a change in volume during isovolumetric contraction. When the left ventricular pressure exceeds the aortic pressure, the aortic valve opens. During left ventricle ejection, left ventricular volume falls. Left ventricle ejection terminates with close of the aortic valve. From the aortic valve close until mitral valve opening, the left ventricular pressure falls without a change in volume (isovolumetric relaxation) [16].

Isovolumetric relaxation ends when the left ventricular pressure decreases below the left atrial pressure. The pressure gradient between atria and ventricle opens the mitral valve and rapid filling of left ventricle begins. Then the pressure gradient continuously decreases and transiently reverses. The reversed mitral valve pressure gradient decelerates and afterward stops the rapid flow of blood into the left ventricle early in diastole. Late in diastole, atrial pressure is increased with atrial contraction and propels the remnant blood into the left ventricle. Finally, the left atrium relaxes and its pressure decreases below the left ventricular pressure. The mitral valve begins closing, and a new cardiac cycle starts [16].

2.2 Action Potential

Myocytes, i.e. the muscle cells of the heart, are surrounded by a membrane composed of a lipid bilayer, which serves as both an insulator and a diffusion barrier to the movement of ions [16]. Diffusion and transportation of ions help establish concentration gradients across the membrane. Because of these gradients the electric potential across the membrane of a myocyte is different, typical value is -90 millivolts. This difference is called transmembrane potential.

An action potential is an event in which the transmembrane potential of a myocyte rapidly rises to positive and gradually falls back to a stable state (resting potential). The whole

event has five phases, 0~4. Phase 0, the shortest phase, is the initial rapid upstroke from the resting potential (typically -80 ~ -90 millivolts) to a positive value (approximately +20 millivolts). The transmembrane potential change in this phase is mainly dependent on sodium, which rushes into the cell through fast Na^+ channels. In phase 1, also known as early repolarization, all fast Na^+ channels are inactivated, and a small amount of K^+ leaks out of the cell and Cl^- leaks in. Thus it brings the potential down to a plateau level in 2 to 3 milliseconds. Next is phase 2, plateau, during which L-type calcium channel current, I_{CaL}, brings Ca^{2+} into the myocyte while the slow delayed rectifier K^+ channel I_{Ks} exudes K^+. Phase 2 accounts for most of the action potential duration, typically lasting around 200-400 msec. Repolarization phase 3 brings the potential back to the resting level, because in this phase the L-type Ca^{2+} channels start to deactivate but the slow delayed rectifier K^+ channels are still open. Phase 4 is resting membrane potential [16]. Depolarization of one myocyte also initiates depolarization of adjacent myocytes through gap junctions and electrotonic coupling [16]. So the depolarization spreads in a wave-like fashion throughout the heart.

Figure 1 shows an example of two recordings of transmembrane potential from a human left ventricular tissue (endocardium side) and a pig right ventricular tissue (endocardium side). From Figure 1, the difference in action potentials of two species is obvious in shape, duration, and amplitude. Even in same species, although the depolarization spreads throughout the heart, there still exist regional differences in action potential shape and duration. This phenomenon has been observed in several animal species and in human heart [17]. The action potential heterogeneity is due to differences in specific electrophysiological properties of cardiac myocytes. Therefore, the heterogeneity should also be taken into consideration in simulation.

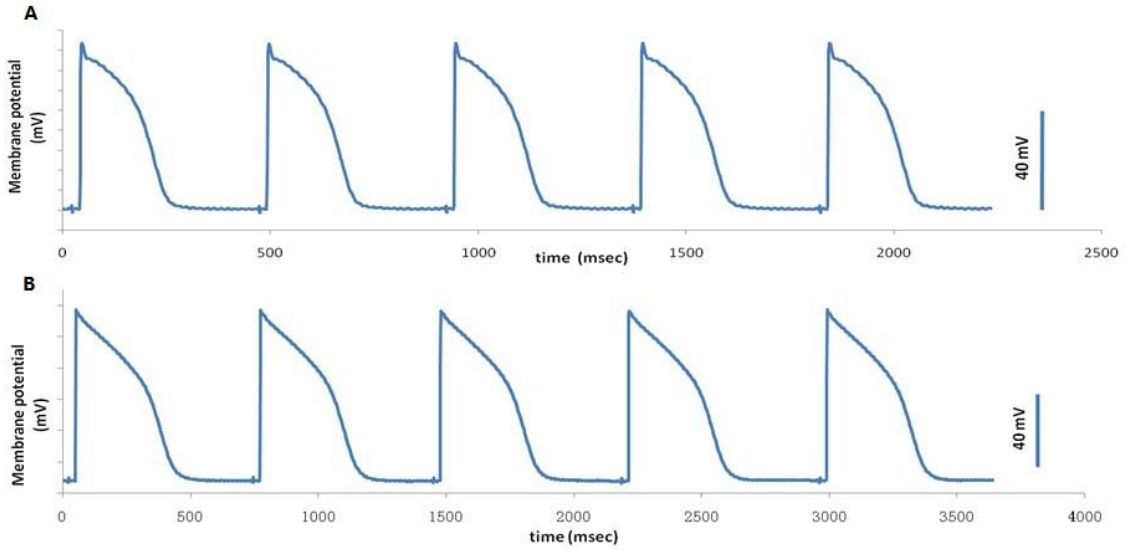

Figure 1 Example of two recording of transmembrane potentials. Top is from endocardium of pig right ventricle, and bottom is from endocardium of human left ventricle.

2.3 Electrocardiogram

Electrocardiogram, also known as ECG or EKG, is the recording of the electrical activity of the heart measured on the surface of the body, typically the thorax. With each heartbeat, the electrical signal spreads from the top of the heart to the bottom. As it travels, the signal causes the heart to contract and relax, and also the potential at one location is different from another. The potential differences can be detected by electrodes attached to the surface of the skin and displayed or stored in a device external to the body.

2.3.1 Morphology of ECG

A typical ECG recording of a heartbeat consists of a P wave, a QRS complex, a T wave, and a U wave. P wave, QRS complex and T wave could easily be recognized by a clinician.

The electrical activity of the heart originates in the sino-atrial node (SA node). During the atrial depolarization stage, the impulse rapidly spreads through the right atrium to the atrioventricular node (AV node). It also spreads through the atrial muscle directly from the right atrium to the left atrium. This spread produces the P wave on the ECG.

Then the electrical impulse travels very slowly through the AV node, very quickly through the bundle of His, and the Purkinje network. The mass of these structures is quite small, so nothing is seen with electrodes on the body surface and the ECG waves are flat.

Finally the wavefront arrives at the ventricular muscle. Depolarization of the right and left ventricles takes a very short period of time, normally 0.06~0.12 second. First area of the ventricular muscle to be activated is the interventricular septum, which activates from left to right. This generates the Q wave. Next, the left and right ventricular free walls, which form the bulk of the muscle of both ventricles, are activated, with the endocardial surface being activated first, followed by the epicardial surface. This activation causes the R wave. A few small areas of the ventricles, close to the boundary of atriums and ventricles, are activated a little late [18]. This generates the S wave. The ventricles normally have a larger muscle mass than atria, so QRS complex shows up with larger amplitude on the ECG.

The last stage is repolarization of ventricular muscle, which generates the T wave. The interval from the beginning of the QRS complex to the apex of the T wave is referred to as the absolute refractory period. The last half of the T wave is referred to as the relative refractory period.

2.3.2 ECG Leads

'Lead' is an ambiguous term in Cardiology. In this document, an ECG lead means the signal of potential difference between two ECG electrodes placed at different locations on the body.

The most commonly used clinical ECG system is the classical 12-lead ECG, which consists of ten electrodes and twelve leads, i.e. there are 12 differences in potentials between these ten electrodes. The twelve leads are called lead I, II, III, aV_R, aV_L, aV_F, V_1, V_2, V_3, V_4, V_5 and V_6.

Of these twelve leads, lead I, lead II and lead III are called limb leads. The electrodes that form these signals are located on the limbs — one on each arm and one on the left leg. The limb leads form the points of what is known as Einthoven's triangle [19,20]. Lead I is

the potential difference between left arm (LA) electrode and right arm (RA) electrode. Lead II is the potential difference between left leg (LL) electrode and RA electrode. Lead III is the voltage between LL electrode and LA electrode. In exercise ECG, the signal is distorted because of muscular activity, and electrode artifacts due to electrode movements. So R. E. Mason and I. Likar suggested putting the electrodes on the shoulders and on the hip instead to minimize effect of muscular activation [20]. For simplicity, we do not include limbs in the model.

Leads aV_R, aV_L, and aV_F are augmented limb leads (prefix 'a' stands for augmented). They are derived from the same three electrodes as limb leads but they view the heart from different angles [19]. Lead aV_R has the positive electrode on the RA electrode and the negative electrode is a combination of LA electrode and LL electrode. Lead aV_R augments the signal strength on the right arm. Similarly, aV_L augments the signal strength of the positive electrode on the left arm and aV_F on the left leg. The projections of the lead vectors of the 12-lead ECG system in three orthogonal planes are illustrated in Figure 2.

For measuring the potentials close to the heart, Wilson introduced the precordial leads (chest leads) in 1944 [21]. These leads, V_1-V_6 are located over the left chest. The points V_1 and V_2 are located at the fourth intercostal space on the right and left side of the sternum; V_4 is located in the fifth intercostal space at the midclavicular line; V3 is located between the points V_2 and V_4; V_5 is at the same horizontal level as V_4 but on the anterior axillary line; V_6 is at the same horizontal level as V_4 but at the midline [22]. Because of their locations close to the heart, they do not require augmentation. The common ground is Wilson's central terminal, which is produced by connecting the electrodes RA, LA, and LL together, via a simple resistive network. Wilson's central terminal approximates an average potential across the body.

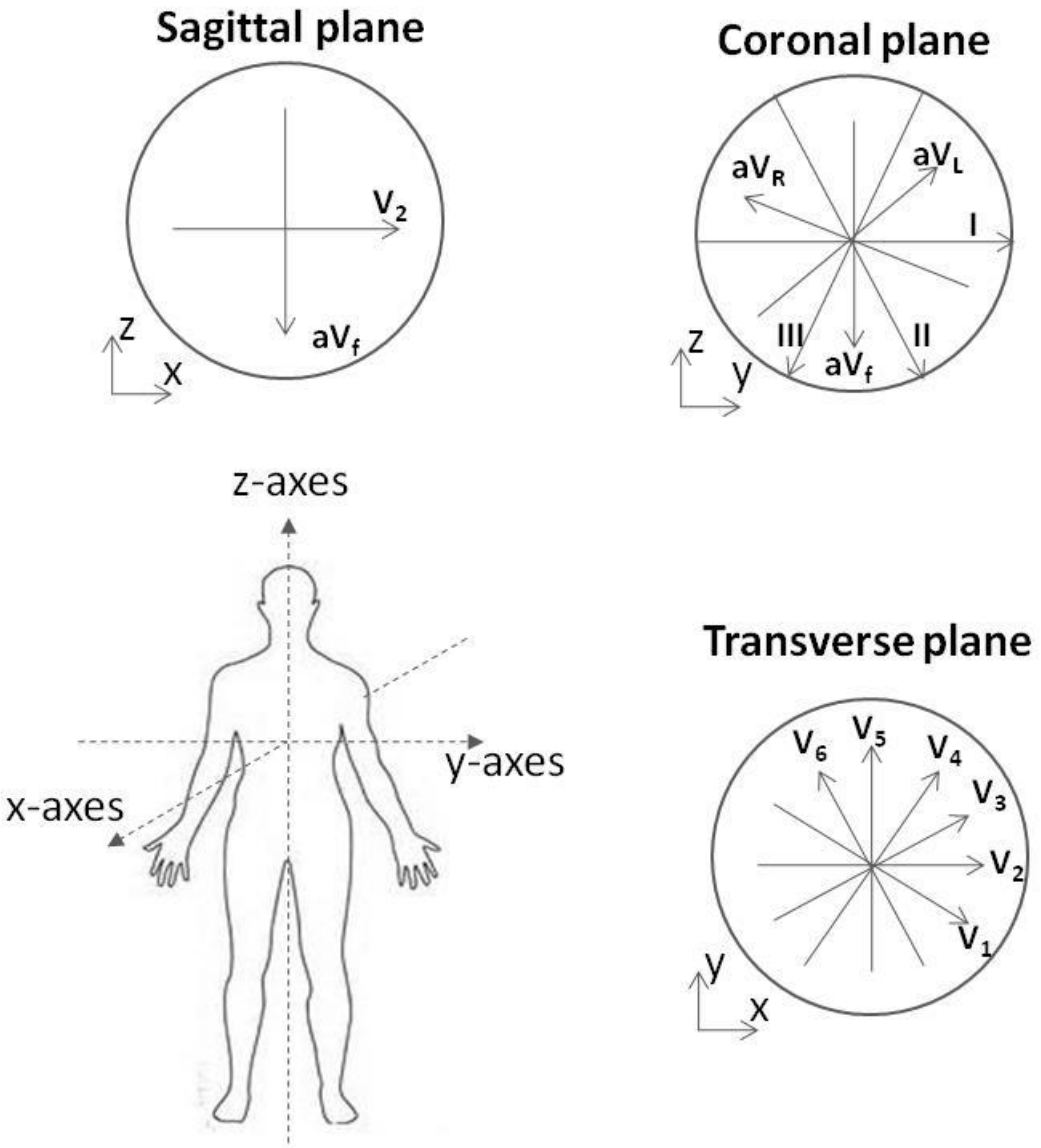

Figure 2 An illustration of the projections of all lead vectors of the 12-lead ECG system in three dimensional orthogonal planes.

For an individual lead, a positive deflection will be seen if a wavefront of depolarization travels towards the electrode attached to the anode of external device and away from cathode. A negative deflection will be seen if the wavefront travels in an opposite direction. A biphasic deflection will be seen if the wavefront travels perpendicular to the line joining the sites where the two electrodes are placed. Based on these principles, we can briefly estimate the waveform of a lead.

For example, since the direction of atrial depolarization, from top left to bottom right, is

roughly parallel to the axis of lead II (60°), a positive deflection (P wave) would result in this lead; the direction of ventricular depolarization is roughly parallel to inverse direction of the axis of lead aV_R, so a negative deflection (reserve R wave) would result in that lead.

The electrophysiological signals mentioned in this section are the signals that we used in our present study. We will describe the detailed methods and techniques in the next section.

CHAPTER THREE: METHODS

3.1 Langendroff Perfusion System

We used the Langendorff heart perfusion method to collect the optical mapping data, which is a widely used approach to study cardiac electrophysiology [23,24]. The experiments conducted were approved by Institutional Animal Care and Use Committee (IACUC) at the University of Kentucky.

Before an experiment, 3L of freshly made modified Tyrodes' solution was prepared and was filtered using a nylon net filter (pore size: 7μm, Millipore). Composition of Tyrode's solution was (in mmol/L) 0.5 $MgCl_2$, 0.9 NaH_2PO_4, 2.0 $CaCl_2$, 137.0 NaCl, 4.0 KCl, and 5.5 glucose. $NaHCO_3$ was added until the pH was between 7.3±0.05. The solution was circulated in the Langendorff perfusion system (see Figure 3), which maintained the solution temperature at 37 °C. The solution was oxygenated with a mixture of 95% O2 and 5% CO2.

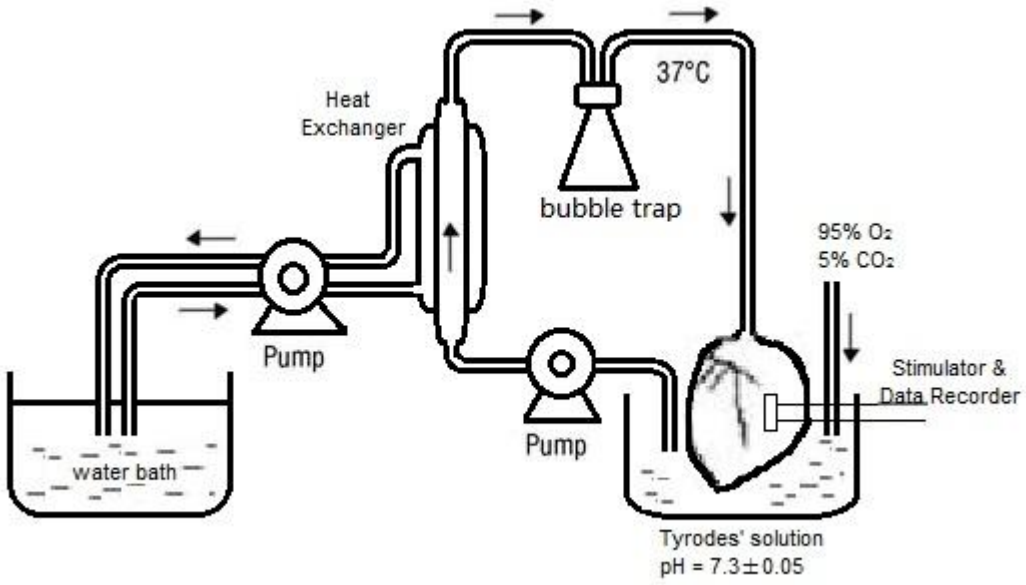

Figure 3 Schematic representation of our Langendorff perfusion setup.

Farm pigs (sus scrofa, 18-20 kg) were anesthetized by an intravenous injection of a combination of Telazol (4-8mg/kg), Ketamine (2-4mg/kg), and Xylazine (2-4mg/kg), followed by thiopental sodium (Pentothal, 10-11 mg/kg) or sodium pentobarbital (40-60

mg/kg). After the pig was completely anesthetized, the thoracic cavity was quickly opened and heart was rapidly excised. Immediately, the heart was immersed in chilled Tyrodes' solution and squeezed mildly to flush out remnant blood. The ascending aorta was cannulated using a short silicone tube (about 50mm long, 20mm diameter).

Finally the heart was placed in a custom-made chamber and the pacing electrodes were gently placed onto heart. The chamber was a transparent plastic box. Pseudo-ECG electrodes were placed on the inside wall of the chamber to approximate three leads of ECG. The base of the heart was on the top and the apex lay towards the bottom of the chamber. The chamber was filled with perfusion liquid. A peristaltic perfusion pump was used for perfusion and the buffer flow rate was adjusted to be about 500 mL/min, which is close to the coronary flow in pig hearts of the size that we used in our studies.

3.2 Data Acquisition

Optical recordings using potentiometric dye were first demonstrated by Salzberg et al. using neurons in 1973 [25]. Voltage-sensitive, i.e. potentiometric, dyes change their spectral properties in response to voltage change of transmembrane potential. Changes in the intensity of emitted fluorescent light are proportional to changes in transmembrane potential. We slowly injected voltage-sensitive dye solution through a T-junction distal to the bubble trap.

A CCD camera (DALSA CA D1 128T) was placed at about 30 cm away from the chamber. We set the camera to record 496 frames per second with a resolution of 128x128 pixels. Four high power green LEDs were put on the side of the chamber so that the heart was in the field-of-view of the LEDs. The room light was turned off, and the green LEDs were turned on and then the epicardial electrical activity was recorded optically. The recording data was acquired by a frame grabber and then sent to a desktop hard disk. Schematic representation of the whole system is in Figure 4.

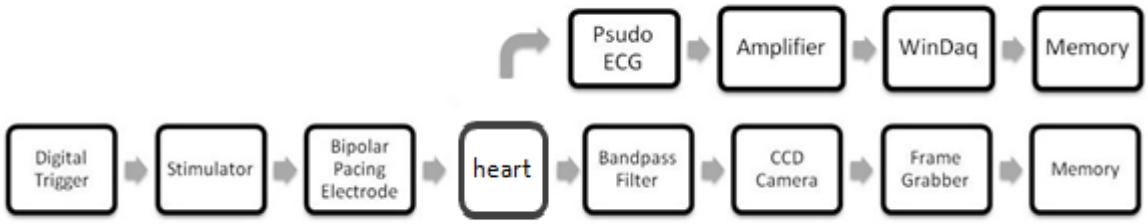

Figure 4 Flow chart of data acquisition system

3.3 Pacing Protocols

Two pacing protocols were used to stimulate the heart. They were constant cycle length protocol, and step function protocol.

Constant cycle length protocol is self-explanatory, which means that within the same recording, the interval between two stimuli was a constant value.

In step function protocol, the cycle length was changed as a step function. The pacing cycle length of first 100 beats was a constant value A. In second 100 beats, the cycle length increased or decreased to another constant value B.

Figure 5 gives an example of the two protocols. Top figure is a constant pacing protocol of 500 ms pacing cycle length. Bottom figure is a step function protocol. First 100 beats was paced at 2 Hz (500 ms cycle length) and next 100 beats was paced at 5 Hz (200 ms cycle length).

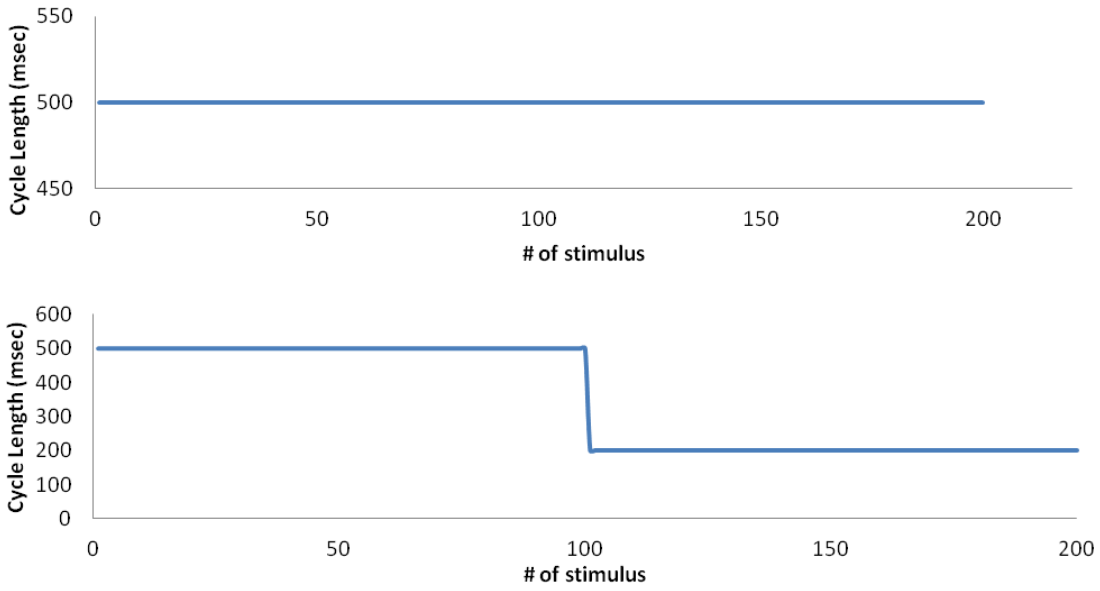

Figure 5 An example of constant cycle length protocol (top), and step function protocol (bottom).

3.4 Heart and Torso Model

3.4.1 Mesh Refinement

In the original model, the surfaces bounding the heart, torso and other organs are triangular meshes. We downloaded the open source files that describe triangulated geometries from Radboud University Medical Center's website [14]. The website provides a tool, called ECGSIM, which enables the user to study the relationship between the electric current sources of the heart and the resulting ECG signals. It provides 3D coordinates of all nodes of a human geometrical model, which includes the heart, the torso and two lungs. The 3D coordinates of the geometrical model were generated from MRI scanning images of human body. In original files, the heart consists of 257 nodes and the torso consists of 300 nodes.

In order to build a smoother surface, we used the loop subdivision algorithm to refine the mesh [26,27]. This algorithm is a recursive subdivision process that refines the mesh into a piecewise linear approximation of a smooth surface. The principle is based on B-spline curve continuity. A B-spline is a piecewise polynomial function of degree k in a variable x. It is defined over a range t 1 ≤ x ≤ tm, m = k + 2. Any spline function on a given

set of nodes can be expressed as a linear combination of B-splines [28].

$$S_{k,t}(x) = \sum_{i} \alpha_i B_{i,k,t}(x)$$

This follows from the fact that all pieces have the same continuity properties, within their individual range of support, at the nodes. Expressions for the polynomial pieces can be derived by means of a recursion formula [28]:

$$B_{j,1}(x) = \begin{cases} 1 & \text{if } t_j \le x < t_{j+1} \\ 0 & \text{otherwise} \end{cases}$$

$$B_{i,k}(x) = \frac{x - t_i}{t_{i+k-1} - t_i} B_{i,k-1}(x) + \frac{t_{i+k} - x}{t_{i+k} - t_{i+1}} B_{i+1,k-1}(x)$$

The algorithm of B-spline curve subdivision has two steps. First, a new node is inserted between two existing nodes. Then the curve is rewritten with the refined node sequence. From Riesenfeld (1975), it is known that under repeated subdivision, the B-spline curve will converge to the underlying curve [26].

Based on the principle of B-spline subdivision, we derived the triangular-splines subdivision. The grid G_i was refined to a grid $G_j = (G_i + G_{i+1})/2$, and update the subsegment of (G_i , G_j) and (G_j, G_{i+1}). Once all grids were updated, this step was repeated. The subdivision procedure was carried out until the distance between any two grid points was smaller than a threshold of 0.02mm.

3.4.2 Source Model

The source model used in the simulation is an equivalent double layer (EDL) on the heart surface S, the surface bounding left and right tissue. The local source strength of any position on the surface is proportional to the transmembrane potential at the same position. Geselowitz (1983) derived this result from an analysis of the electrical properties of ventricular cells treated as a homogeneous syncytium by using bidomain model [29]. In his paper he gave the equation of source model:

$$\varphi(\vec{y}) = -\int_{vol} g_i \, \nabla\varphi_m \, (\vec{x}) \, \nabla Z \, dv$$

where $\varphi(\vec{y})$ is the potential at position $(\vec{y})$ outside the heart, g_i is the conductivity of the

intracellular aspect of the bi-domain, ∇ the gradient operator, $\varphi_m(\vec{x})$ the transmembrane potential at all points $\vec{x}$ throughout the heart, and $Z = Z(\vec{y}, \vec{x})$ is the lead field of the electrode configuration involved. In other words, $Z(\vec{y}, \vec{x})$ is the property of a pair of a source point on the heart surface and an observation point on the torso, which is reciprocal of the distance between $\vec{x}$ and $\vec{y}$ [30].

By applying vector calculus to the previous equation, Geselowitz transferred the equation to:

$$\varphi(\vec{y}) = -\int_S g_i \varphi_m(\vec{x}) \nabla Z \, dS$$

Especially for potentials φ_∞ in a hypothetical, infinite homogenous medium surrounding the heart, Z can be expressed as:

$$Z(\vec{y}, \vec{x}) = \frac{1}{4\pi\sigma R}$$

where σ is the conductivity of the medium and R is the distance between $\vec{y}$ and $\vec{x}$. Boundary condition is $g_i \varphi_m(\vec{x}) \nabla Z \, dS = 0$.

In words, this equation expresses the summation of the contributions to the external potential of all local transmembrane potential differences present throughout the entire volume of the ventricular tissue.

3.4.3 Forward Transfer Problem

'Forward' and 'inverse' problems are two terminologies used to describe two typical problems in electrocardiography. The forward problem entails the calculation of body surface potentials, starting from either the source model that represent the heart's electrical activity or from known potentials on epicardium, usually optical mapping data. On the contrary, the inverse problem tries to optimize the parameters of source model so that the computation results of body surface potential distribution most closely match the measured heart's electrical activity [31-33]. Since the objective in our model was to

estimate ECG based on measured optical mapping data, we needed to solve the forward problem.

Surface method and volume method are two widely used approaches for forward problem. In surface method, it assumes the different torso regions are all of isotropic conductivity and only the boundaries between different torso regions are represented in the numerical torso model [34]. In volume method, however, not only surface but also the entire torso model is represented numerically by finite elements. Volume method needs more complex torso models so that more elements and potentials need to be determined, while surface method uses simpler torso model with fewer elements. Since we wanted to simulate and display 12-lead ECG almost in real time, plus the torso model we used did not have many elements, we chose the surface method in this study.

Surface method is based on partial differential equations for the potential on the finite element mesh of the torso surface. The equations can be expressed as [34]:

$$\nabla\sigma(\nabla\Phi) = 0 \text{ in } \Omega$$

$$\Phi = \Phi_0 \text{ on } \Gamma_H$$

$$(\sigma \nabla\Phi)\, n = 0 \text{ on } \Gamma_T$$

where Γ_H is epicardial surface boundary, Γ_T is torso surface boundary and Φ_0 is transmembrane potential on the epicardial surface boundary.

3.4.4 Depolarization Sequence

During sinus rhythm, the wave of depolarization spread through the heart is an orderly process. Generally, as mentioned in the previous chapter, it begins at the SA node and spreads rapidly through the right and left atria and reaches the AV node, where it encounters an expected delay. The impulse then travels rapidly through the bundle of His and the Purkinje fibers. Purkinje fibers radiates toward the myocardial fibers, stimulating them to depolarize and contract.

To estimate the depolarization sequence, we focused on the optical mapping recording made during pacing at 500 ms cycle length, because 500 ms is close to the duration of a

normal pig heart beat. A threshold was used to determine the electrophysiological activity status of cells within the area of a pixel so that all the cells in this pixel were considered to be depolarized if the brightness of this pixel was greater than the threshold, otherwise they were considered to be at repolarization stage. Comparing the onset of depolarization at each pixel to stimulus artifact allowed us to compute the local average conduction delay. Connecting pixels which had the same conduction delay was used to make the contour map plot of iso-chronal activation. Therefore, using this approach we could estimate the timing of depolarization for each node in the model.

3.5 Software Development

Development environment used in our model was mainly Qt OpenGL and visual studio 2012. OpenGL is a multi-platform application programming interface (API) for rendering 3D vector graphics. It is just a standard API and provides little support for graphical user interface (GUI) programming issues. The user interface for an OpenGL application must be created with another toolkit. We used Qt because it is a cross-platform application and UI framework that is widely used for developing application software with a GUI. Qt uses standard C++ but makes extensive use of a special code generator together with several macros. Open-source version installers of Qt 5.2.0 and Qt creator were downloaded online [35].

One of the key modules we used in the program was Qt OpenGL module. It provides an OpenGL widget class that can be used just like any other traditional Qt widget and makes easier to use OpenGL in Qt application. Its basic functionality is very similar to Mark Kilgard's GLUT library [36], but it can take advantages of the Qt API GUI functionality.

We used Visual Studio 2012 as the compiler.

The program consists of three subwindows and other parameters. The top left widget is heart model. Its orientation can be changed in X, Y or Z direction freely by pressing the left mouse button and dragging the mouse, and its scaling can be changed by pressing the left mouse button and scrolling back and forth. The color of each point on the surface represents the transmembrane potential at that position. A pre-computed index color map

is used to convert the potential value to its corresponding color. Blue (hex value is #0000FF) refers to resting potential while red (hex value is #FF0000) refers to peak potential.

The bottom left subwindow is torso. It shows the placement of 12-lead ECG electrodes. By clicking on the black dot and dragging the mouse, one can slightly change the placement of a single electrode. If the left mouse button is pressed on white area and the mouse is moved, the back side of torso model can be seen. On the right side is the ECG subwindow. It consists of twelve subwindows. Each subwindow is inherited from QwtPlotCanvas class. So the green solid line represents one of the twelve channels of 12-lead ECG signals. The horizontal yellow dash line represents the baseline and the vertical yellow solid line indicates the time stamp.

Structure of the whole program is illustrated in Figure 6.

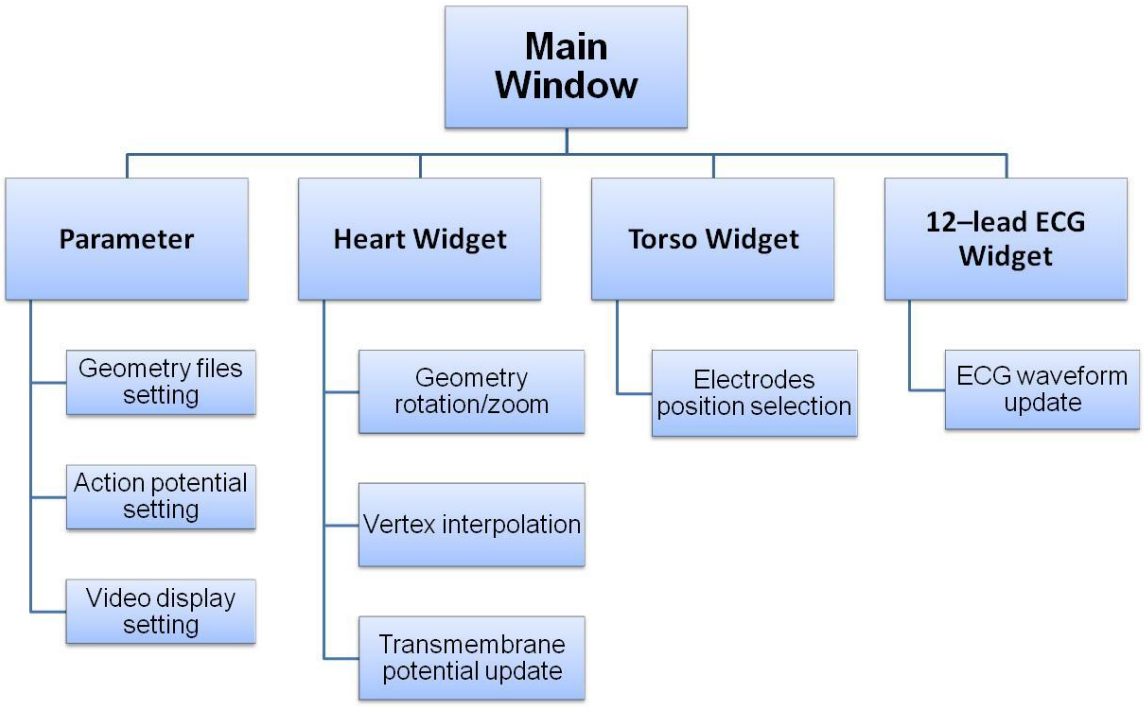

Figure 6 Structure of the model.

CHAPTER FOUR: RESULTS

4.1 Optical Mapping Data Processing

The optical mapping data stored in hard drive cannot be directly used in our model, because raw optical data included unwanted background and often has low signal-to-noise ratios. So there were several steps that were employed to improve signal quality.

When we imaged the hearts using our optical imaging system, we usually adjusted the camera's field of view a little wider than the tissue preparation so that the entire preparation was visible in the screen. Therefore, all the frames we extracted from optical data file contain a combination of foreground pixels (preparation) and background pixels. Background contains noise that can skew data analysis and must be removed at the very first step. So a preprocess step is necessary for reducing noise. The preprocess started by importing first 3000 frames of images, followed by computation of cumulative peak-to-peak difference for each pixel in all frames. Changes in brightness in foreground area was proportional to changes in transmembrane potential while background always remains dark, or the intensity of the background does not change appreciably. The peak-to-peak difference in foreground pixels' intensity was very different from that between the background pixels (Figure 7 left). Thus, the background was segmented by creating a binary mask. The pixel value was set to logical '1' if its peak-to-peak value was greater than the threshold, otherwise the value was set to '0' (Figure 7 middle). Appropriate morphology operations, image dilation and image erosion, were used on the binary mask to fill tiny holes and remove noise. Then this mask was applied to each frame in the sequence (Figure 7 right).

Figure 7 Example of mask generation. The process involved importing first 3000 frames of images, followed by computation of cumulative peak-to-peak difference for each pixel in all frames. Results of this operation are plotted in the left panel. The red area is approximately the position of the heart. After this step, an appropriate threshold was selected so that image on the left is converted to a binary image (middle). After applying image morphology operation to the binary image, the tiny holes were filled and noise reduced.

Once the region of interesting had been extracted from background, two types of digital filters were used to improve optical signal quality. One was spatial filter and the other was temporal filter. The spatial filter that was used was a two dimensional filter. We convolved each frame with a Gaussian kernel to reduce high frequency noise and aberrant pixels. Then a low-pass temporal filter was applied to a sequence of frames to attenuate the influence from background light change and other noise, such as baseline drift. We tried multiple sizes of kernel and moving window length before deciding on an optimal size and length. We decided to select 5X5 Gaussian kernel (σ=1) because it seems to remove most of the noise but still maintain details as determined by manual inspection. Average moving window filter was selected as the low-pass temporal filter, since it had acceptable performance and less computation time. Length of moving window was 9 points such that signal to noise ratio was largest. Outputs resulting from these operations are shown in Figure 8 and Figure 9.

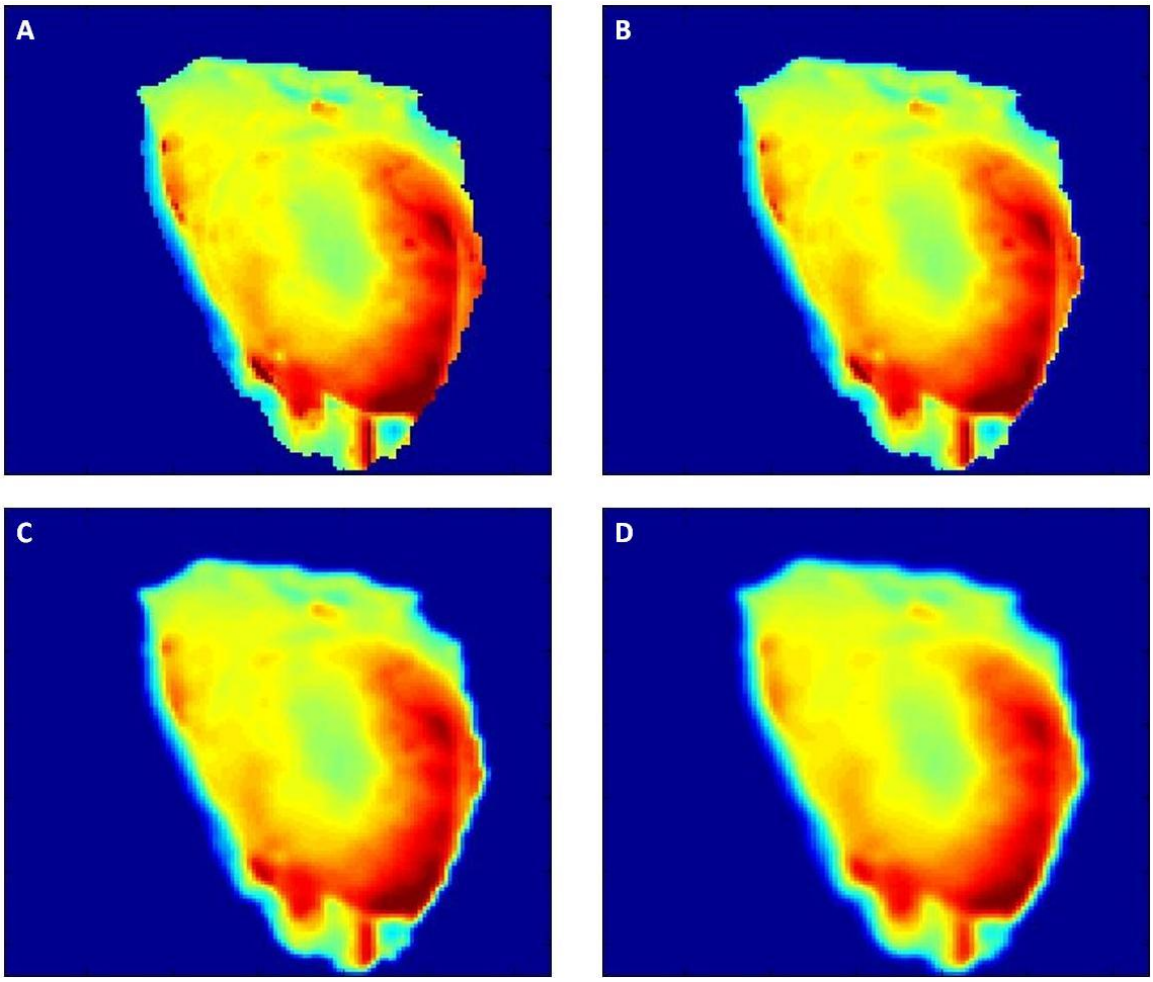

Figure 8 Original image (A) and output of three spatial filters (B, C, and D). All three filters used were rotationally symmetric Gaussian low-pass filters with standard deviation = 1. Sizes of these filters were 3x3, 5x5 and 7x7, respectively.

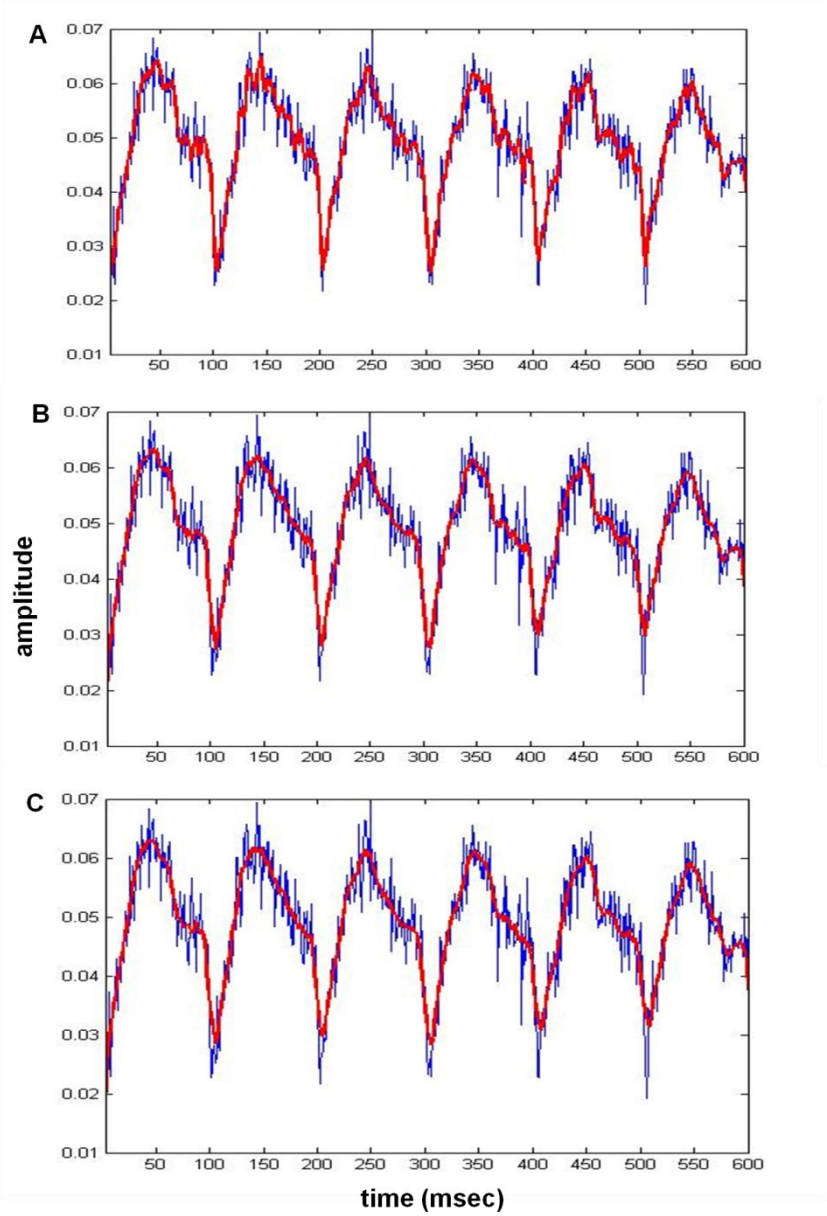

Figure 9 The output of moving average filters with length of moving window of 7 points (A), 9 points (B), and 11 points (C). These are values of one specific pixel extracted from 3000 successive frames. Blue solid line represents the original noisy signal and red solid line represents the filtered signal. Note that the optical signals were acquired at very high rates of activation (nearly 10 Hz) which is reflected in the shapes of action potentials being different from what is seen at slower rates.

4.2 Re-entry Arrhythmia

The pacing electrode was placed on the left side of the heart. Depolarization was initialed at the position of pacing electrode, and then propagated to adjacent cells so that the

adjacent region of the heart depolarized as well.

Normally the conduction velocity at one location is close to that of a small region nearby and depolarization propagates on the heart surface in uniform direction. For example, at pacing rate of 2 Hz (500 ms), the depolarization wave started from left and propagated to right, as illustrated in first two rows of Figure 10.

However, if the pacing rate is abnormal, due to the electrical properties difference of a small local region, the depolarization sometimes would be conducted by both a fast path and slow path. At fast pacing rate, after a new stimulus follows closely to the previous one, the fast pathway probably is still refractory and conduction is by the slow pathway. The depolarization wave by slow pathway reaches intersection may find the fast pathway and loop back upon itself.

When the pacing rate was increased, for example, to 5 Hz (200 ms), a re-entry event happened. In third and fourth rows of Figure 10, the figure shows that at lower left portion of the heart the conduction velocity was extremely slow or even blocked. So the depolarization wave was conducted through a fast pathway, close to atria, up to the beginning of the slow pathway. This conduction resulted in re-entry.

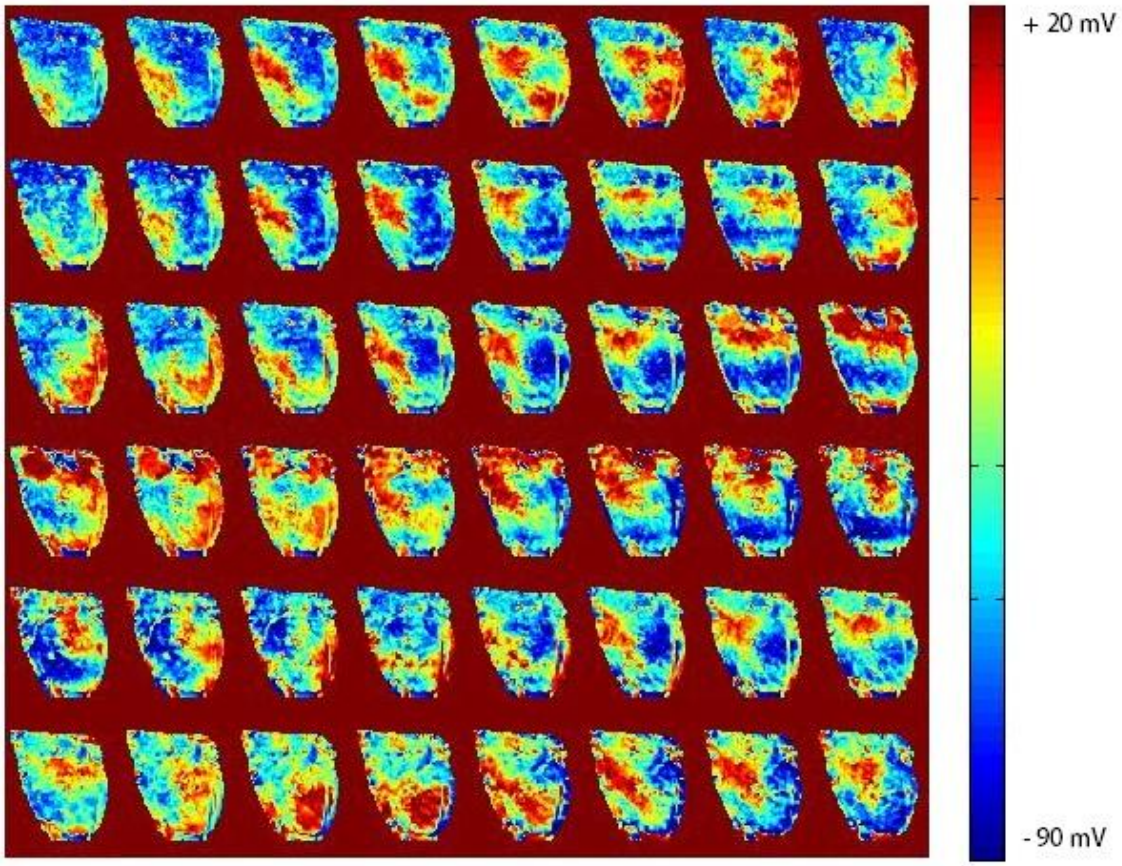

Figure 10 In first three rows, pacing rate is 2 Hz (500 ms cycle length) and depolarization propagation is unidirectional. Then pacing rate increased to 5 Hz (200 ms cycle length), the electric signal wave did not complete the normal circuit (from left to right), but rather an alternative circuit looping back upon itself (last three rows). This conduction of depolarization wave resulted in re-entry.

4.3 Geometric Model Refinement

The original model of human heart, downloaded from the website, contained six geometry files, one for epicardium, one for torso, two for left and right ventricles and another two for left and right lungs. The format of geometry files is consistent with the universally accepted geometry definition file OBJ. The first line of each file contains two integers, n the number of vertices and m, the number of triangular faces. In the following n lines, each row is the XYZ coordinates of a vertex. Next m lines are the vertex indexes of all faces stored in a counter-clockwise order. The coarse mesh of heart consists of 257 vertices and 510 faces, and torso mesh consists of 300 vertices and 596 faces. The initial

coarse polygon mesh is plotted in Figure 11, including front view (left) and side view (right).

The coarse mesh was repeatedly refined into a sequence of increasingly dense meshes following the method mentioned in the previous chapter, until the maximum distance between any two vertices was less than a threshold (2 mm in this case). After several repeats, the heart and two ventricles' meshes were divided into a total of 4082 vertices and 8160 faces so that the entire heart was much smoother than before. The torso mesh was divided into 1194 vertices and 2384 faces. Figure 12 shows the refined geometric model. First row is torso mesh and second row is heart mesh.

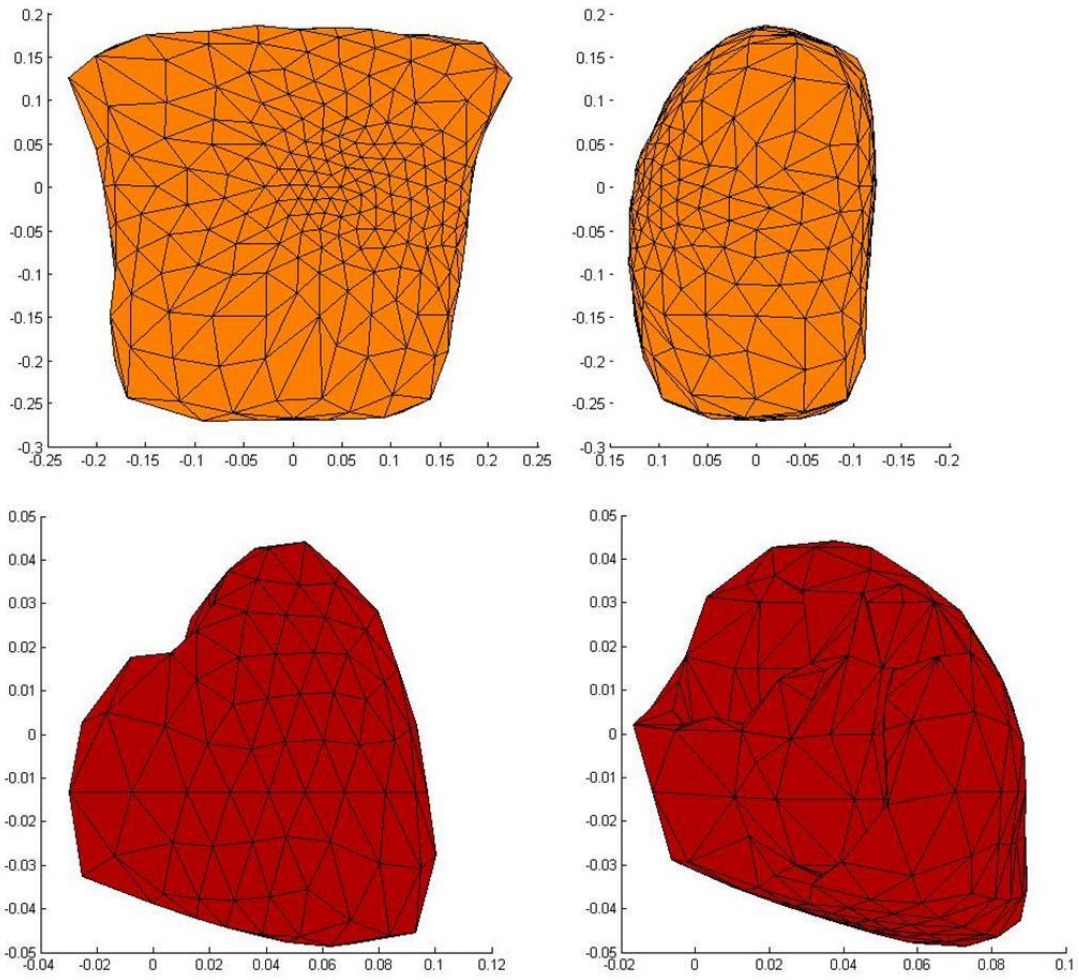

Figure 11 Original geometric models. Top is the orthographic projection of torso, front view (top left) and side view (top right). Torso polygon mesh consists of 300 vertices and

596 faces. Bottom is the orthographic projection of heart, front view (bottom left) and top view (bottom right). Heart polygon mesh consists of 257 vertices and 510 faces. Unit of all X and Y axes is meter.

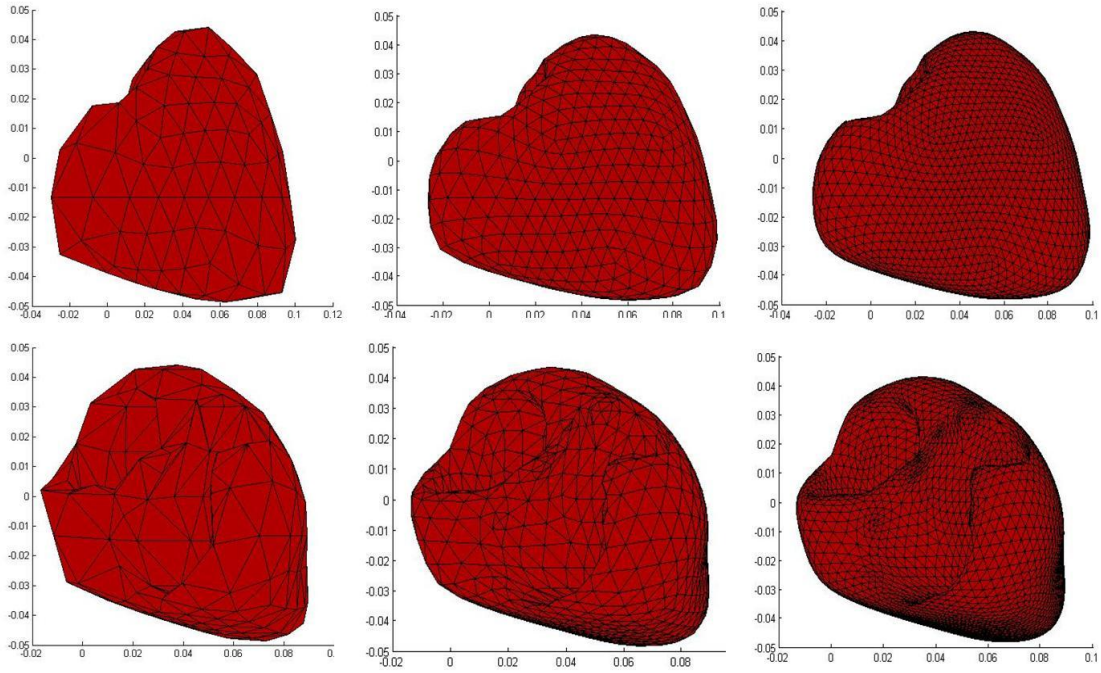

Figure 12 Loop subdivision of heart polygon mesh. As the distance threshold decreases, the number of vertices and faces increase, and the mesh looks smoother. From left to right, the number of vertices is 257, 1022, 4082, and the number of faces is 510, 2040, 8160, respectively.

4.4 ECG Simulation

User interface of this application is very straightforward. Main window is shown in Figure 13. As mentioned before, top left is the subwindow of heart model and bottom left is the subwindow of torso model. Black dots on surface of torso indicate the locations of electrodes. Right of the window is twelve subplots of all channels of 12-lead ECG signals.

There are three items in the menu bar. By clicking ‘File’ button, one can import optical data files from external disks or export ECG simulation results to external storage. Next to it is ‘Edit’ button. Clicking ‘Edit’ button accesses the ‘Parameter Setting’, ‘Geometry Setting’ and ‘Display Setting’ panels to adjust model parameters, reload geometry files

and change display format. User interface of panels is shown in Figure 14.

Values of action potential duration and maximum dv/dt are changeable in the model. Therefore the heterogeneity could be taken into consideration in simulation. The initial values are set as displayed in the panel, and consequent 12-lead ECG signals are in Figure 13.

Just below the menu bar, there is another bar with three buttons. The button on the left is used to control start or stop of the simulation. The button in the middle is used to run the simulation step by step. The button on the right can reset the simulation and start over again.

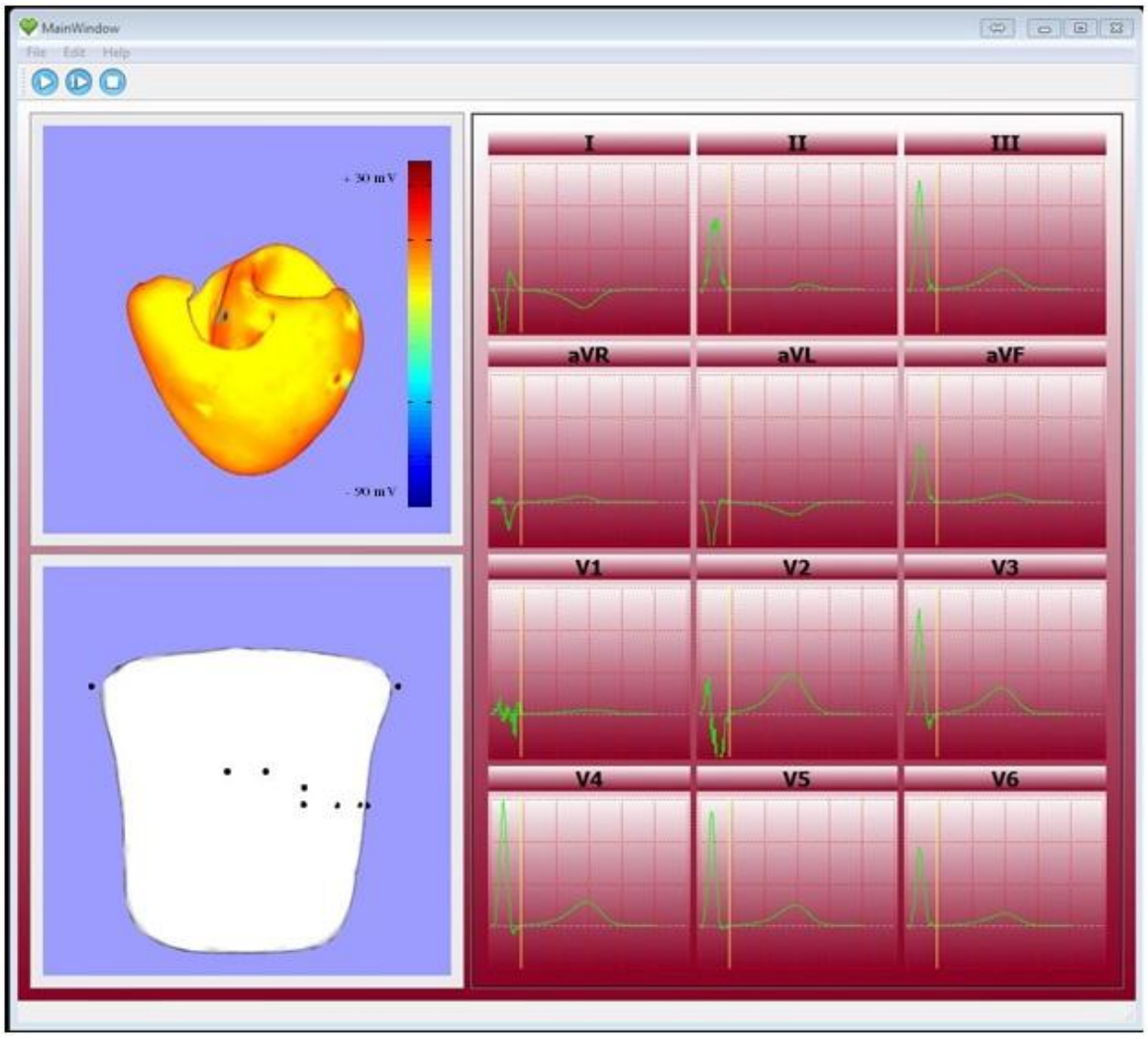

Figure 13 Main window of the application.

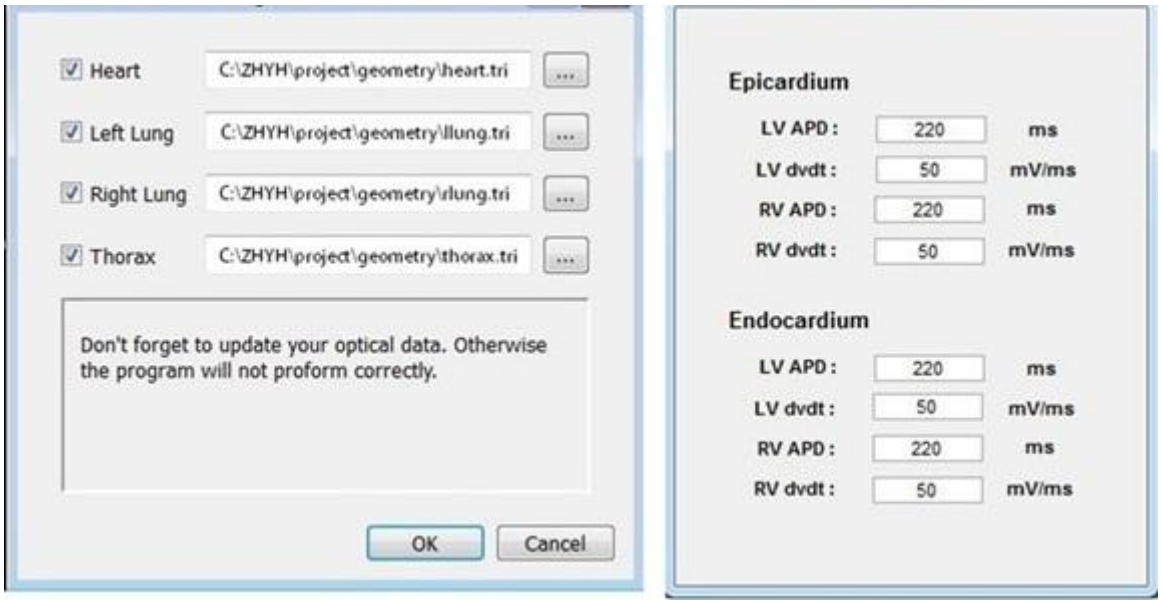

Figure 14 User interface of ‘Geometry Setting’ panel (left) and ‘Parameter Setting’ panel (right).

CHAPTER FIVE: DISCUSSION

5.1 Model Development

In this section, we compare the one dimensional signal analysis and two dimensional image processing methods used in the model with other popular methods.

5.1.1 Temporal Filtering Selection

In the previous section, we applied moving average filter for noise reduction in time domain because of its simple design and ease of implementation [37]. Moving average filter can be in the form of simple moving window where all bins are equally weighted or in the form of a weighted moving window where different weights are assigned to bins at different positions of the window. The window shape (weights) and window size need to be adjusted according to the amount of high-frequency components. As shown in Figure 9, the wider the moving window is, the fewer high-frequency components remain.

To design a filter, the pass band and stop band of the filter should be determined first. By taking the Fourier transform of the same pixel in a sequence of frames, we observed that the dominant frequency spectrum is below 50 Hz. So the ideal filter in this circumstance is a low-pass filter that keeps most of the signal between 0~50 Hz and attenuates frequency components above 50 Hz as much as possible. There are two classical types of digital filters other than moving average filter: infinite impulse response (IIR) and finite impulse response (FIR).

In general, FIR filter's impulse response is of finite duration, while IIR filter may continue to respond indefinitely and have internal feedback. Usually FIR filters are simple to design and are guaranteed to be stable. An IIR filter can be unstable if not designed properly compared to FIR filter. Also, FIR filters have linear phase characteristics whereas IIR filters do not have linear phase. IIR filters, however, are useful for high-speed designs, because they typically require a lower number of coefficients compared to FIR filters [38].

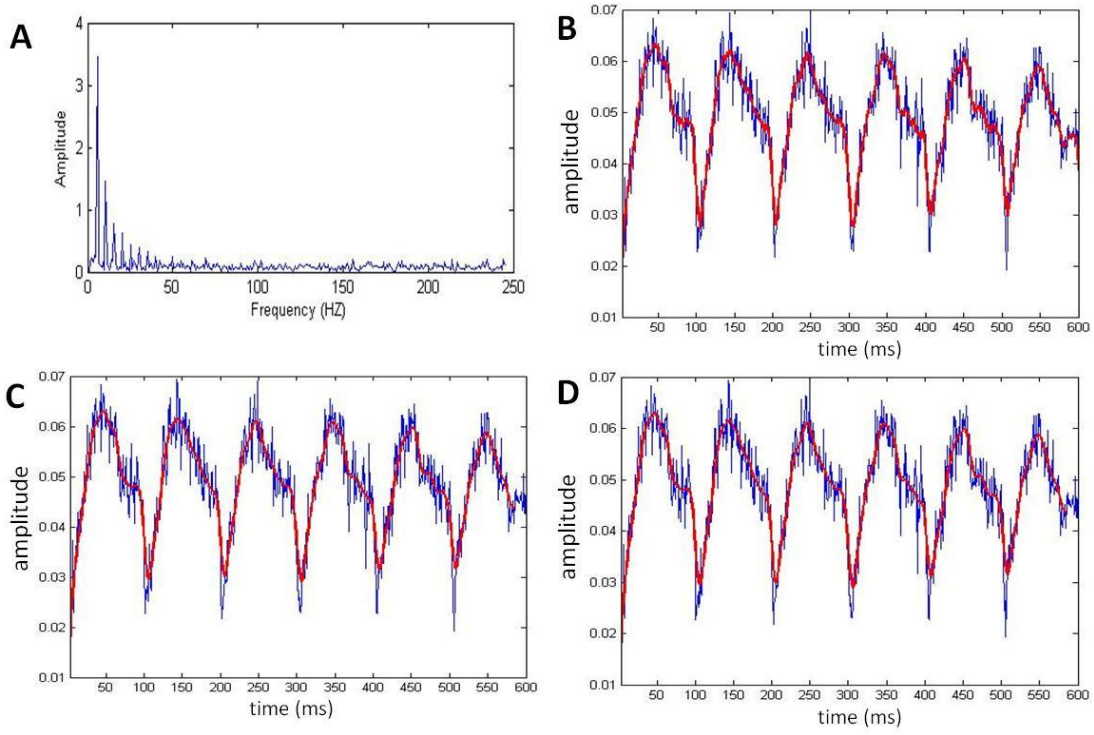

Figure 15 Frequency spectrum of signal (A), original signal and output of 9 points moving average filter (B), 24 order FIR filter (C) and 24 order Butterworth IIR filter (D).

Figure 15 demonstrates the output of a moving average filter, a Butterworth IIR filter and a 24^{th} order FIR filters. For cardiac mapping data processing, based on our manual inspection, all filters can be applied for successful filtering, and there is no significant difference in the outputs of three types of filter. However, the characteristic trade-offs of filters should be taken into account when choosing an appropriate filter, such as phase delay or computation consumption. In our model, we used the efficient and easily implemented moving average filter, i.e. an FIR filter.

5.1.2 Surface Interpolation

Surface interpolation is another operation that was used in the model. The purpose of surface interpolation was to approximate transmembrane potentials at all nodes from a set of scattered points. Those scattered points were converted from pixels in optical imaging data, so transmembrane potentials of those points were proportional to the brightness of corresponding pixels. The transmembrane potentials of other nodes would be estimated on the basis of those known scattered points as well.

To estimating potentials at other nodes, the widely used methods could be divided into two classes: global interpolation and local interpolation. The global interpolation is aimed at finding a smooth surface so that all measured scattered data points are distributed evenly on both sides of the surface, and the sum of distances of measured points to the surface is minimum. Values of other nodes are calculated based on this smooth surface. In two dimensions, the smoothness functions are [39]:

$$\varepsilon_1 = \int f_x^2(x,y) + f_y^2(x,y)dxdy = \int ||\nabla f(x,y)||^2 dxdy$$

and

$$\varepsilon_2 = \int f_{xx}^2(x,y) + 2 * f_{xy}^2(x,y) + f_{yy}^2(x,y)dxdy$$

The smaller $\varepsilon 1$ and $\varepsilon 2$ is, the smoother the surface is. However, to find the minimum costs a lot of computation power.

Local interpolation is relatively simple. Interpolated value just depends on neighboring known scatter points. Therefore, if the weighted coefficients are saved in a lookup table, once the value of known scatter points update, the value of rest points are able to be recalculated in a constant time (O(1) time complexity).

Since the surface of model was triangular mesh, barycentric coordinates system could use three floating numbers to represent any node in a triangular mesh. The values of floating numbers were proportional to the areas of three subtriangles. Areas of the three subtriangles could be calculated by using Heron's formula. So barycentric interpolation would be more convenient to operate with triangular mesh than other two dimensions interpolation methods, like spline interpolation. As shown in Figure 16, since the surface of heart was of three dimensions, the new point P was possibly located outside the plane of ABC. So the first step was to project point P onto plane of ABC. Projection point was marked as P' and its xyz coordinators could be computed from P and normal vector of plane ABC. Then by using the coordinates of A, B, C and P', the areas of ΔABP', ΔACP', and ΔBCP' could be calculated easily. Three weighted coefficients of points P were reciprocal of areas of three triangles. Coefficients of all vertices were stored in a constant

array. Thus time complexity of update reduced to a linear time (O(n) time complexity).

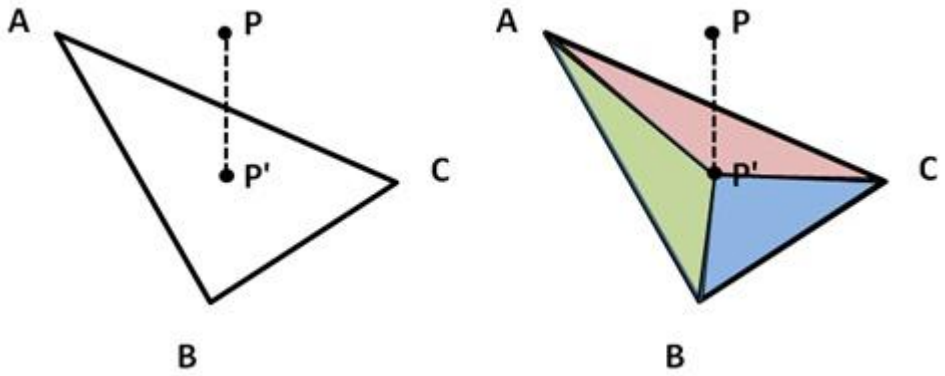

Figure 16 Demonstration of barycentric interpolation. Value of Point P is determined by A, B, C and the distance of its projection to AB, BC, AC.

5.2 Potential Uses of the Developed Model

5.2.1 Optical Recording Visualization

Optical recording of isolated perfused heart is one of major techniques used in electrophysiological and biological research studies using animal hearts [23, 25]. It allows the investigation of cardiac contractile strength, coronary blood flow regulation, cardiac metabolism and cardiac electrical activity with an intact, but isolated, animal heart. In particular, it is a predominant method for studies of depolarization propagation pathway, conduction velocity and heterogeneity on the surface of heart.

By using conventional method, i.e. processing optical data frame by frame, the electrophysiological information can be analyzed and be displayed in a 2D image format, as shown in Figure 17. In our model, it not only is able to generate figures which contains similar information (such as activation start and complete sequence) as Figure 17, but also can redisplay the entire recording as a 3D animation. Our model provides a vivid visualization of the entire electrophysiological event.

What is more, by importing data to this model, the body surface potential could be calculated by solving the forward transfer problem and displayed on the screen. It overcomes the disadvantage of more widely used optical mapping methods where

synchronous ECG signals are not available from the experiment data. Of course, the computed ECGs are simulated, therefore, the accuracy of these simulated signals depends on appropriateness of the conductivities and geometry that is used.

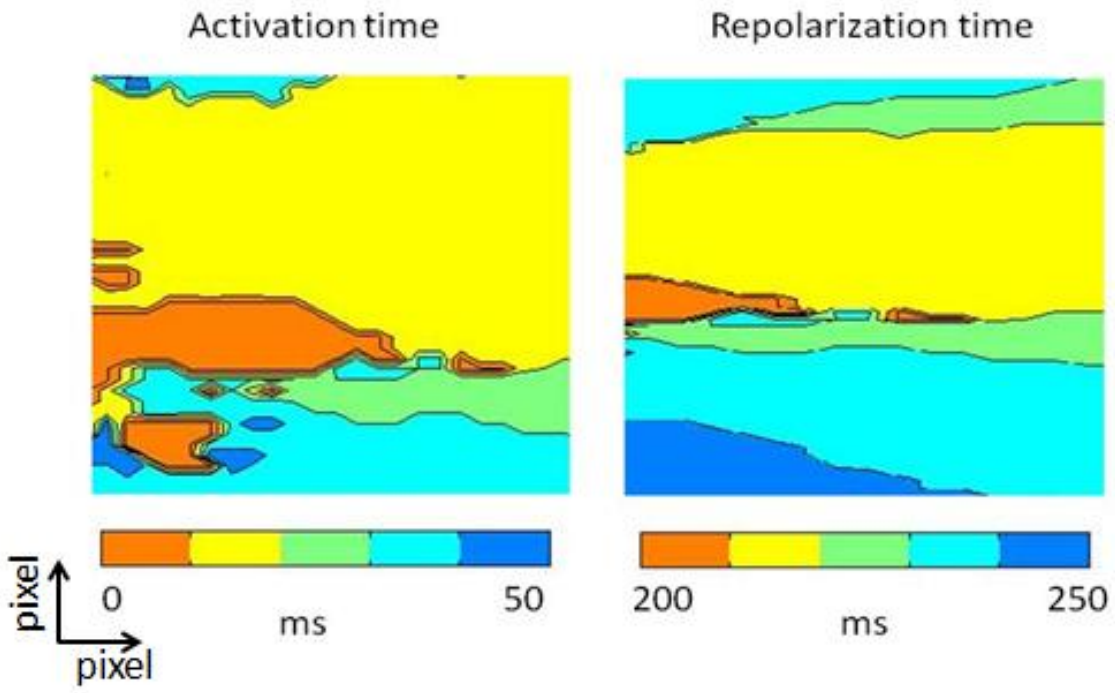

Figure 17 Isochronal maps of activation start time (left) and repolarization completion time (right).

5.2.2 QT Interval Estimation and Long QT Syndrome

In cardiology, the QT interval is a measurement of the duration of electrical depolarization and repolarization of the ventricles. Many researchers consider that a lengthened QT interval, to some extent, is an indicator for potential of ventricular arrhythmias and a risk for sudden death [40,41].

Prolonged QT interval could be due to an adverse drug reaction [42] among other factors. With tissue experiments, one can inject the specific drug into the circulation buffer and record its effect on action potentials, but the changes in ECG waveform are not easy to deduce from these studies. While conducting a noninvasive animal experiment, the ECG signals could be acquired easily, but the effect of drug on target is difficult to visualize directly. With our model, we could modify local action potential properties according to the

results of tissue experiments and simulate the consequent ECG signals. For example, we recorded the transmembrane potentials of cardiac tissues from different regions of animal heart. Then we set the action potentials properties in one specific region in our heart model the same value as the experimental results from the corresponding region of the animal heart. Therefore if action potential properties changed in one region of the heart, the model should be able to reflect the consequent changes in ECG signal. Prolongation of QT interval could also be due to long QT syndrome, which is a rare inherited heart condition [43]. Similar to assess the effect of drug, one can record optical mapping data at a specific location on the heart from genetically modified animals. Then one could import the data in our model to replace the data at the same location on the healthy heart. Therefore our model can help determine whether genetic modification at one location would lead to long QT syndrome.

5.2.3 Defibrillation Investigation

Defibrillation is a common treatment for life-threatening arrhythmia, such as ventricular fibrillation. In 1947, Dr. Claude Beck, at Case Western Reserve University, first successfully used an electrical shock for defibrillation. A high alternating voltage was delivered to the exposed heart by two metal paddles. Later, implanted defibrillator was developed and the high alternating voltage power source was replaced by a large capacitor. The success rate of defibrillation increased. However, there is still open an important question: what is the optimal timing of shock delivery during fibrillation and where is the optimal place of shock.

Ventricular fibrillation is a high risk event, and also defibrillation electrical shock causes damage to the hearts. Animal studies are widely used to study defibrillation phenomenon. Our model can partly replace some procedures in the animal experiments. For example, first, one could make an optical recording when the Langendroff perfused heart is fibrillating. Then the saved data can be imported to our model. After simulation, the resulting ECG waveform looks similar to typical fibrillation ECG. Then it may be possible to add a strong electrical shock at different time and location, and then repeat the calculation of consequent ECG waveform until the fibrillation ceases. Thus these results

can help in determining optimal timing and location of shock. It is acknowldeged that the application of a defibrillation shock is not a feature built in the model at this time and these types of studies will require modification of the model to incoroporate the effects of electrical shocks.

CHAPTER SIX: LIMITATIONS

Improvements of the model can be made at various points. First of all, we included the geometrical model of left and right ventricle, while left and right atria play an important role in generation of the P wave. So in our simulation results we just see QRS complex and T wave but no P wave. In order to reflect a complete ECG, finite elements of atrium should be included in the geometrical model. Electrical and mechanical properties of atriums also need to be taken into consideration.

Another limitation is the heterogeneity of action potential duration throughout the cardiac tissue. In the previous studies from our group that were used in the development of this model, only one high speed camera was used. Therefore, we were unable to record 360 degree view of the isolated heart. For the model, in the areas which were not covered by camera, the action potential shapes were estimated based on our previous results and the sequence of depolarization based on spread of activation. However, our previous tissue experiments have shown spatial heterogeneity in the shape, duration, and other properties of action potentials. So more sample locations are required to improve the accuracy of electrical conduction path prediction, and thus the surface body potentials.

In addition, the structure of the torso model could have an effect on the potential conductivity. The torso model we used is highly simplified. Therefore, if we want to simulate more realistic body surface potential to compute ECG, we should consider the effects of other organs and depth of fat, and a more refined geometry of both heart and torso as well.

To build a more realistic model, there is a need to improve the structure of model itself and to collect more experimental data to verify the model.

REFERENCES

[1] John RM, Tedrow UB, Koplan BA, et al. Ventricular Arrhythmias and Sudden Cardiac Death. Lancet, 380(9852): 1520-9.

[2] Apoor S. Gami, et al., Obstructive Sleep Apnea and the Risk of Sudden Cardiac Death: A Longitudinal Study of 10,701 Adults. Journal of the American College of Cardiology, 2013. 62(7): P610-616.

[3] Umesh C Sharma, Nirmal Kharel, Yeong Shyan Lee, et al. Cardiac MRI Identifies the Possible Cause of Cudden Cardiac Arrest in More Than 50% of Resuscitated Patients. J Cardiovasc Magn Reson. 2013; 15 (Suppl 1): P254.

[4] J R Parga, N M IKari, L N P Bustamante, et al. MRI Evaluation of Congenital Coronary Artery Fistulae. British Journal of Radiology, Volume 77, Issue 918.

[5] Krishna S Nayak, Charles H Cunningham, Juan M Santos, et al. Real-time Cardiac MRI at 3 Tesla. Magnetic Resonance in Medicine, April, 2004, 51(4): 655-660.

[6] T Stan Greory, Ehud J Schmidt, Shellley Hualei Zhang and Zion Tsz Ho Tse. 3DQRS: A Method to Obtain Reliable QRS Complex Detection Within High Field MRI Using 12-lead Electrocardiogram Traces. Magnetic Resonance in Medicine, Aprial 2014, 71(4): 1374 -1380.

[7] Sebastian Weingartner, Mehmet Akcakaya, Sophie Berg, et al. Improved 3D Late Gadolinium Enhancement MRI for Patients with Arrhythmia or Heart Rate Variability. Cardiovasc Magn Reson, 2013, 15 (Suppl 1): P29.

[8] Melissa Bailey, Gwynne Kirchen, Bridget Bonaventura, et al. Intraoperative MRI Electrical Noise and Monitor ECG Filters Affect Arrhythmia Detection and Identification. J Clin Monit Comput, 2012, 26: 157-161.

[9] Jia P, Punske B, Taccardi B, Rudy Y. Electrophysiologic endocardial mapping from a noncontact nonexpandable catheter: a validation study of a geometry-based concept. J Cardiovasc Electrophysiol, 2000, 11(11), 1238-51.

[10] Fuller MS, Sandor G, Punske B, et al. Estimates of repolarization dispersion from electrocardiographic measurements. Circulation, 2000, 102(6), 685-91.

[11] A. Van Dam PM, Oostendorp TF, Linnenbank AC, van Oosterom A. Non-Invasive Imaging of Cardiac Activation and Recovery. Annals of Biomedical Engineering 2009, 37(9):1739-56.

[12] Wu R, and Patwardhan A. Mechanism of Repolarization Alternans Has Restitution of Action Potential Duration Dependent and Independent Components. Journal of Cardiovascular Electrophysiology, 2006, 17(1): 87-93.

[13] Wu R, and Patwardhan A. Effects of Rapid and Slow Potassium Repolarization Currents and Calcium Dynamics on Hysteresis in Restitution of Action Potential Duration. J Electrocardiology. 40(2): 188-99. 2007.

[14] ECGSIM website, http://www.ecgsim.org/index.php

[15] Qt OpenGL website, http://www.qt-project.org/doc/qt-5/index.html

[16] Matthew N. Levy, Bruce M. Koeppen, Bruce A. Stanton, Principles of Physiology, 2010, sixth edition.

[17] Jing L, Chourasia, Patwardhan A, Heterogeneous Memory in Restitution of Action Potential Duration in Pig Ventricles. Journal of Electrocardiology, 2010. 43(5): 425-432.

[18] Richard E. Klabunde. Cardiovascular Physiology Concepts, 2nd Edition. Williams & Wilkins, 2011, ISBN: 9781451113846.

[19] H. C. Burger, J. B. Van Milaan, Heart-Vector and Leads. Br Heart Journal, 1946. 8(3): 157-161.

[20] Mason RE, Likar I., A New System of Multiple-lead Exercise Electrocardiography. American Heart Journal, 1966. 71(2):196–205.

[21] Wilson, Frank N., et al., The Precordial Electrocardiogram. American Heart Jounary, 1944. 27(1): 19-85.

[22] Jaakko Malmivuo, Robert Plonsey, Bioelectromagnetism: Principles and Applications of Bioelectric and Biomagnetic Fields. Oxford University Press, New York, 1995.

[23] Qing Luo, Wenwen Li, Igor R., Efimov. Multiparametric Optical Mapping of the Langendorff-perfused Rabbit Heart. J. Vis. Exp. 2011(55), e3160.

[24] Jacob I. Laughner , Fu Siong Ng , Matthew S. Sulkin, et al., Processing and Analysis of Cardiac Optical Mapping Data Obtained with Potentiometric Dyes. Heart and Circulatory Physiology, 2012. 303: H753-H765.

[25] L B Cohen, B M Salzberg, A Grinvald, Optical Methods for Monitoring Neuron Activity. Annual Review of Neuroscience, 1978. 1: 171-182.

[26] R. F. RIESENFELD, On Chaikin's Algorithm, Computer Graphics and Image Processing, 1975. 4: 304-310.

[27] C. T. Loop. Smooth Subdivision Surfaces Based on Triangles. M.S. Thesis, Department of Mathematics, University of Utah, August 1987.

[28] Jos Stam, Evaluation of Loop Subdivision Surface.

[29] David B. Geselowitz, W. T. Miller III, A Bidomain Model for Anisotropic Cardiac Muscle. Annals of Biomedical Engineering, 1983. 11(3-4): 191-206.

[30] A van Oosterom, Genesis of the T Wave as Based on An Equivalent Surface. Journal of Electrocardiol, 2001. 34S: pp217-227.

[31] Tang Fa-Kuan, Wang Qian, HUa Ning, et al., Forward and Inverse Problem for Cardiac Magnetic Field and Electric Potential Using Two Boundary Element Methods. Chinese Physics B, 2010. 19(12) 120601.

[32] G.T. Lines, M.L. Buist, P. Grottum, A.J. Pullan, J. Sundnes, A. Tveitoet al., Mathematical Models and Numerical Methods for the Forward Problem in Cardiac Electrophysiology. Computing and Visualization in Science, 2003. 5(4): 215-239.

[33] Burton, B.M., Erem, B., Potter, K., Rosen, P., et al., Uncertainty Visualization in

Forward and Inverse Cardiac Models. Computing in Cardiology Conference (CinC), 2013.

[34] Charulatha Ramanathan, Yoram Rudy, Effect of Torso Inhomogeneties on Body Surface Electrocardiographic Potentials. Journal of Cardiovascular Electrophysiology, 2001. 12(2): 229-241.

[35] Qt 5.2.0 Open Source download, http://qt-project.org/downloads.

[36] GLUT, the OpenGL Utility Toolkit, http://www.opengl.org/resources/libraries/glut/.

[37] Lee, P., Bollensdorff, C., Quinn, T. A., Wuskell, J. P., Loew, L. M., & Kohl, P. Single-Sensor System for Spatially Resolved, Continuous, and Multiparametric Optical Mapping of CardiacTtissue. Heart Rhythm, 2001. 8(9), 1482-1491.

[38] Louis Litwin, FIR and IIR Digital Filters: the Effects of Finite Bit Precision.

[39] Marroquin, J., Mitter, S., & Poggio, T., Probabilistic Solution of Ill-posed Problems in Computational Vision. Journal of the American Statistical Association, 1987. 82(397), 76-89.

[40] Day C P, McComb J M, Campbell R W. QT Dispersion: An Indication of Arrhythmia Risk in Patients with Long QT Intervals. British Heart Journal, 1990, 63(6): 342-344.

[41] Schwartz, P. J., Moss, A. J., Vincent, G. M., & Crampton, R. S. Diagnostic criteria for the long QT syndrome. An update. Circulation, 1993, 88(2), 782-784.

[42] Andrew Leitch, Peter McGinness, David Wallbridge. Calculate the QT Interval in Patients Taking Drugs for Dementia. BMJ, 2007, 355(7619): 557.

[43] Wang, Q., Shen, J., Splawski, I., Atkinson, D., Li, Z., Robinson, J. L., . & Keating, M. T. SCN5A mutations associated with an inherited cardiac arrhythmia, long QT syndrome. Cell, 1995, 80(5), 805-811.

VITA

Education

Bachelor of Engineering in Biomedical Engineering, Zhejiang University, China

Professional Experience

Assistant Researcher, Samsung Advanced Institute of Technology, Beijing, China (2014.03 ~2014.06)

Assistant Researcher, Sogou, Inc. , Beijing, China (2014.06 ~ now)